Theoretical investigation of electron dynamics driven by laser pulses in graphene nanoribbons

Rulin Wang [1,*] Fuzhen Bi,[2] Wencai Lu,[1] Xiao Zheng,[3] and ChiYung Yam[4]

[1]*College of Physics, Qingdao University, No. 308 Ningxia Road, Qingdao, 266071, China*
[2]*Qingdao Institute of Bioenergy and Bioprocess Technology, Chinese Academy of Sciences, Qingdao, 266101, China*
[3]*Hefei National Research Center for Physical Sciences at the Microscale,*
University of Science and Technology of China, Hefei, Anhui 230026, China
[4]*Beijing Computational Science Research Center, Haidian District, Beijing, 100193, China*

Control of electron dynamics in graphene nanoribbons (GNRs) is critically important for the future applications of graphene-based nanoelectronic devices. Based on real-time simulations, we investigate the manipulation of electronic transport by femtosecond laser pulses in armchair GNRs. The simulation results show that the multiphoton absorption process can drive the photon-excited electron flow along a GNR. The corresponding transferred charges are determined by the order of multiphoton absorption and depend on the central frequency and energy distribution of few-cycle laser pulses. Furthermore, the transferred charge can be controlled by the carrier-envelope phase of pulses; this dependence vanishes as the duration time of laser pulses increases. These results also provide insights into the manipulation of electron dynamics using lasers and the design of optoelectronic devices based on graphene materials.

I. INTRODUCTION

The manipulation of electron dynamics at the atomic scale is a key issue for the design of next-generation electronic devices [1,2]. This ultrafast dynamic phenomenon can be realized with the photoexcitation of electronic devices by few-cycle laser pulses [3–5]. The development of modern laser technology makes it possible to control the waveform of the pulses in experiments [6–8]. The transient electric field of laser pulses leads to electron dynamics, which causes a current across the electronic devices. While this electron dynamics and transient current are usually too fast to measure experimentally, the time-integrated current (transferred charge) is more relevant for the measurement of electron dynamics. Combined with the ultrahigh temporal resolution of laser pulses, the measurements of transferred charge through scanning-tunneling-microscopy (STM) junctions have been developed to detect real-time dynamic phenomena in picosecond and femtosecond timescales, such as molecular vibrations [9], single-molecule structural transitions [10], the relaxation dynamics of surface plasmons [11], and electron dynamics in molecules [12,13]. In these nanojunction systems, the transferred charge can be controlled by the carrier-envelope phase of laser pulses [14–17] and the gap width of the junctions [11,18]. For semiconductor devices with a band gap, the photoexcitation induced by the pulses should be related to the band gap of the system. The dependence of electron dynamics and transferred charge on the band gap requires further investigation.

Graphane nanoribbons (GNRs) have gained considerable attention due to their potential application for future nanoelectronic devices [19]. The electronic properties of GNRs can be adjustable according to the structural engineering by bottom-up molecular assembly [20,21]. For example, zigzag GNRs exhibit edge magnetism with ferromagnetic ordering localized at the NR edge, which indicates their good application prospects of zigzag GNRs in spintronics [22–24]. Armchair GNRs exhibit a controllable band gap depending on the widths of the NRs, which indicates their potential application in optoelectronic devices [25–27]. For bilayer armchair GNRs, a continuous change of band gap has been realized by applying a vertical electric field [28].

Previous studies of the photoresponse focused on the steady photocurrent along the GNRs under stable light illumination [29–32]. In such photoelectronic devices, atomic-level doping technology was employed to fabricate *p-n* junctions, and the built-in electric field around the junction interface drives the separation of photoexcited electron-hole pairs, which is an indispensable step in generating photocurrent in steady states. In this paper, we consider the transient photoresponse in armchair GNRs driven by the few-cycle laser pulses, for which the intensity of incident light varies in the femtosecond time domain. Instead of the steady photocurrent induced by the built-in electric field, we investigate transient photocurrent and corresponding transferred charge originating from an asymmetric electric field of laser pulses in pure GNRs without local doping atoms.

To calculate the real-time electron dynamics, we use the practical scheme of time-dependent simulation for open systems [33–35], and the transient electronic properties of open systems are characterized by closed equations of motion for the reduced single-electron density matrix [36–41]. The part

---

*rulin11@qdu.edu.cn

of GNRs under illumination is taken as an open system in which the electrons are excited to nonequilibrium states by external laser pulses. The other parts of the GNRs are treated as surrounding environments that provide the dissipative channels for the nonequilibrium states of open systems. The influence of dissipative processes between systems and environments is accounted for with an energy- (ϵ-)dependent spectral function $\Lambda(\epsilon)$. $\Lambda(\epsilon)$ at each energy point is related to the characterized relaxation time of electron dynamics.

In the framework of the nonequilibrium Green's-function (NEGF) method, a set of linearly coupled equations of motion is established to simulate the electron dynamics of an open system and each equation of motion corresponds to an energy point of $\Lambda(\epsilon)$ [36]. This inevitably results in huge computational costs that are difficult to achieve in practical simulation. One way to improve computational efficiency is proposed in the simulation of electron dynamics occurring at around the Fermi energy, which is known as a wide-band-limit (WBL) approximation, in which $\Lambda(\epsilon)$ is assumed to be energy independent and a constant spectral function at the Fermi energy is used [42]. In the photoexcitation processes of GNRs, especially for armchair GNRs with a band gap, the electron dynamics away from Fermi level plays important roles in the simulation. Here, we adopt a Lorentzian decomposition scheme in which the ϵ dependence of $\Lambda(\epsilon)$ is taken into account and $\Lambda(\epsilon)$ is decomposed by Lorentzian functions; each Lorentzian function corresponds to an equation of motion [36,37,40].

The rest of this paper is organized as follows. In Sec. II, we describe the simulation details of electron dynamics in armchair GNRs and demonstrate the accuracy of the Lorentzian decomposition scheme. In Sec. III, the control of transient photocurrents and transferred charge by the waveform of laser pulses is investigated and the dependence of electron dynamics on the band gap of armchair GNRs presented. Finally, Sec. IV concludes the paper with a summary of simulation results obtained in this work.

II. SIMULATION DETAILS

We consider a photoelectric device of an armchair GNR with width $W = 0.74$ nm (i.e., $N = 7$), as shown in Fig. 1(a). The supercell includes 14 carbon atoms and extends along the x axis with infinite length. The external laser pulses irradiate on the part of the GNR involving six supercells ($L = 6$, the blue-shaded region). A discussion of different lengths L of the irradiation area will be given further below. The electric field of pulses is polarized along the NR, which would drive the region under irradiation out of equilibrium. In our simulation, this irradiation area of the GNR is taken as an open system, and the electron dynamics is obtained by the equation of motion for the reduced single-electron density matrix $\boldsymbol{\sigma}_D(t)$:

$$i\dot{\boldsymbol{\sigma}}_D(t) = [\boldsymbol{h}_D(t), \boldsymbol{\sigma}_D(t)] - i\boldsymbol{D}(t), \tag{1}$$

where $\boldsymbol{h}_D(t)$ denotes the Hamiltonian of the open system and $\boldsymbol{D}(t)$ the dissipative processes from the open system to the left- and right-hand sides of the GNR. The term $\boldsymbol{D}(t)$ plays a dominant role in the simulation of a photocurrent, which provides a dissipative channel for the electron dynamics of the
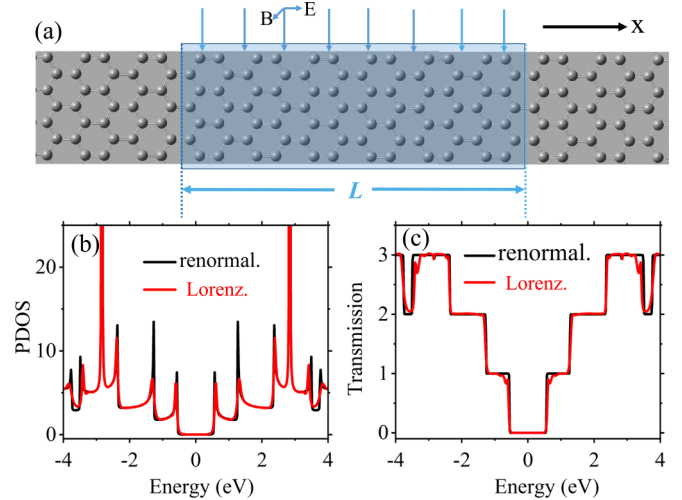

FIG. 1. (a) Schematic of armchair GNR; the atoms under irradiation constitute the open system (blue-shaded part). Simulation results with and without the Lorentzian decomposition approach for the (b) projected density of states and (c) transmission.

open system and results in time-varying photocurrents across the NR: $\boldsymbol{I}(t) = -Tr[\boldsymbol{D}(t)]$.

Employing the NEGF scheme, the $\boldsymbol{D}(t)$ is represented by the spectral function $\Lambda(\epsilon)$ [37], which can be obtained by a highly convergent renormalization algorithm [43] for quasi-one-dimensional systems, such as the NR system described in this work. In this case, the spectral function is expressed as an $n \times n$ matrix and the dimension n is the number of atomic levels in the open system. To reduce computational cost, the Lorentzian decomposition approach is employed to decompose $\Lambda(\epsilon)$ with Lorentzian functions

$$\boldsymbol{\Lambda}(\epsilon) = \sum_{i=1}^{N_l} \frac{1}{(\epsilon - \Omega_i)^2 + W_i^2} \bar{\boldsymbol{\Lambda}}_i. \tag{2}$$

Here, N_l is the number of Lorentzian functions used in the decomposition, Ω_i (W_i) the center (width) of the ith Lorentzian function, and $\bar{\boldsymbol{\Lambda}}_i$ the corresponding coefficient parameters. Without loss of generality, every element of the spectral function matrix is fitted using Lorentzian functions with the same centers Ω_i and widths W_i. The parameters $\bar{\boldsymbol{\Lambda}}_i$ are determined by a least-squares fit to $\Lambda(\epsilon)$. Thus, the time-dependent nonequilibrium Green's-function (TD-NEGF) approach is formulated by a set of closed equations of motion, and the computational cost and number of equations is related to the number of Lorentzian functions N_l. The details of the derivation can be found in our previous works [36,37,41].

In this calculation, the electronic structures of GNRs are described by a nearest-neighbor tight-binding Hamiltonian. The on-site energy of each atom is set to $\epsilon = 0$ for the equilibrium state and the energy ϵ would vary with the electric field of pulses and be determined by the position of the atoms. The carbon-carbon bond lengths are set to 1.42 Å. Owing to the hydrogen passivation of edge carbon atoms, the coupling strength at the edge of armchair GNRs is increased by 12% [23]. Therefore, we set the nearest-neighbor coupling

strengths to $\gamma_0 = -2.7$ eV [44] and $\gamma_e = 1.12\gamma_0$ for interior carbon atoms and edge atoms, respectively.

The accurate description of the spectral function $\Lambda(\epsilon)$, used to represent the electronic structure of the environment and provide the dissipative paths for electron movement, is crucially important in the simulation of transient current occurring at the boundary between the open system and environment. The fitting Lorentzian functions are centered at 40 equally spaced energy points and the widths W_i are set to the same value as the energy interval of these spaced points. To examine the accuracy of reproducing $\Lambda(\epsilon)$ with Lorentzian decomposition, we calculate the projected density of states (PDOS) and transmission of the open system at equilibrium. Figures 1(b) and 1(c) show the simulation results with Lorentzian decomposition ($N_l = 40$) compared to the results obtained without Lorentzian decomposition. It can be clearly seen from the figures that the curves agree with each other very well, both for the simulation of PDOS and transmission. In other words, for the system considered in this work, Lorentzian decomposition can capture the overall features of the electronic structure of the environment and the dissipative paths through the designated boundary. We employ Lorentzian decomposition to simulate the electron dynamics of GNRs in the following sections.

III. RESULTS AND DISCUSSIONS

Next, we investigate the transient properties of the system driven by the external laser pulses. The pulses are assumed to be linearly polarized and the polarization is parallel to the GNR direction. The electric field is considered an AC source to avoid the influence of the DC component on the calculation results [16,18]. Thus, the vector potential of laser pulses is given by $A(t) = (E_0 T)/(2\pi) \exp[-t^2/(2\sigma^2)] \sin(2\pi t/T + \varphi)$. The waveform of pulses can be controlled by the electric field amplitude E_0, period time T, duration time σ, and carrier-envelope phase (CEP) φ of the incident laser. The electric field is obtained as follows: $E(t) = -\dot{A}(t)$.

A. Influence of irradiation region size on transient photocurrent

In the beginning, the GNR system stays at thermal equilibrium. At a certain time, a laser pulse ($E_0 = 0.8$ V/nm, $T = 10$ fs, $\sigma = 0.5T$, $\varphi = 0$) irradiates the part of GNR that includes six supercells ($L = 6$) and 84 carbon atoms. Experimentally, this nanometer scale irradiation region may be realized with field enhancement around the narrow gaps between metal nanoparticles and sharp tips in colloidal gold particles [45]. Figure 2(a) shows the time-varying electric field of the pulse and the positive (negative) values denote fields pointing to the right (left). During the time period in which the electric field is applied [−15, 15 fs], the field drives the GNR out of equilibrium. After the electric field is applied ($t > 15$ fs), the electronic response of the GNR dissipates so that the system relaxes back to the equilibrium state. The electron dynamics is calculated with the electron density matrix equation [Eq. (1)], and the transient photocurrent is obtained using the dissipation term $I(t) = -Tr[\boldsymbol{D}(t)]$, as shown in Fig. 2(b). The corresponding time-varying transferred charge is calculated by $Q_{tr}(t) = \int_{-\infty}^{t} I(t')dt'$ and plotted in Fig. 2(c).
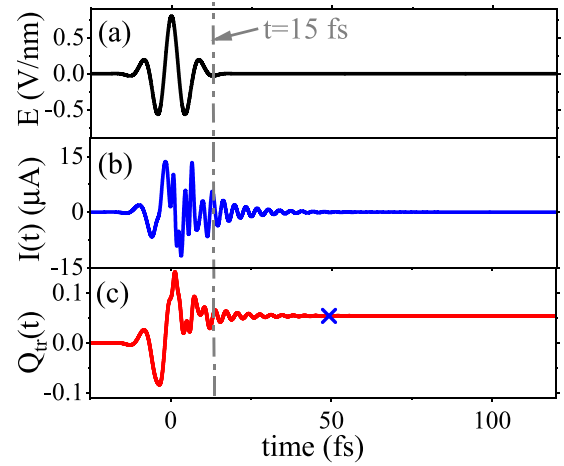

FIG. 2. (a) Time-varying electric field of laser pulse with $E_0 = 0.8$ V/nm, $T = 10$ fs, $\sigma = 0.5T$, and $\varphi = 0$. (b) Transient photocurrent and (c) time-dependent transferred charge flowing along the GNR induced by the laser pulse. The irradiation region length is $L = 6$.

In the same way, we simulate the electron dynamics of systems with different irradiation-region lengths ($L = 8, 10, 12$) and plot the calculation results of $Q_{tr}(t)$ in Fig. 3. Comparing these curves with the results in Fig. 2(c), at $t < 0$ fs, the four irradiation-region conditions give the same line shape of transferred charge. This relies on the fact that, at the beginning of applying the field, the electron exchange between the irradiation area and other parts of the GNR is mainly determined by the electron dynamics around the boundary. As time goes on, the electrons from the center of the irradiation area propagate to the boundary and result in the difference of $Q_{tr}(t)$ varies with the length L. When the equilibrium is restored, the transferred charges tend to positive constants, i.e., $Q = Q_{tr}(\infty)$, which indicates the total charge transfer from the left-hand side to the right-hand side of the GNR induced by the laser pulses due to the asymmetry of the electric field with much larger positive values. The total transferred charges Q are
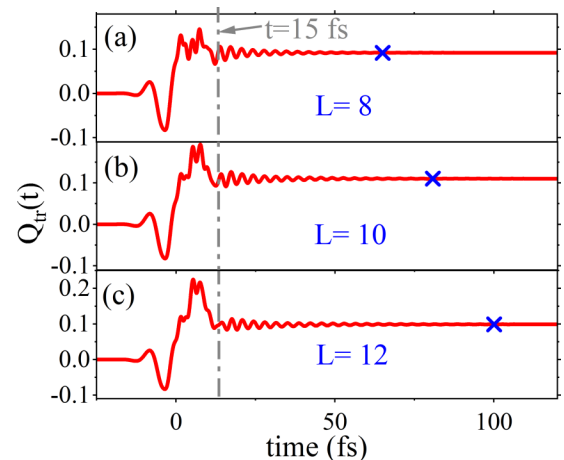

FIG. 3. Time-dependent transferred charge flowing along the GNR with different irradiation region lengths: (a) $L = 8$, (b) $L = 10$, and (c) $L = 12$.

$0.054e$, $0.092e$, $0.11e$, and $0.099e$ for $L = 6$, 8, 10, and 12, respectively. The overall increasing trend of the transferred charges Q is due to higher potential gaps between the two ends of the irradiation region as the length L increases.

From the perspective of time domain, Q is mainly established at the driven part (-15 fs $< t < 15$ fs) of the electron response by laser pulses, while the relaxation part ($t > 15$ fs) has almost no contribution to transferred charge. The fluctuations in the relaxation part represent the intrinsic properties of the system and the frequency is equal to the band gap of the GNR (1.14 eV). A characteristic relaxation time τ_d can be defined as the time that the amplitude of the transient photocurrent is less than 0.1 μA. The relaxation time τ_d [blue points in Figs. 2(c) and 3] is 49, 65, 82, and 100 fs, corresponding to $L = 6$, 8, 10, and 12, respectively. It is clear that the time τ_d is proportional to the lengths L because more relaxation time is needed for the photoexcited electron dissipating into the surrounding environment as the lengths L increase.

The real-space manipulation of the motion of electrons is crucially important to the development of modern electronics. Hereafter, we focus on the control of the transferred charge Q by the waveform of a single laser pulse, and show the dependence of Q on the band gap of an armchair GNR system.

B. Manipulation of transferred charge by CEP and duration time of laser pulses

We now investigate the dependence of transferred charge Q on the CEP of single laser pulses, the simulation results have been plotted in Fig. 4. The other parameters of pulses are set to $E_0 = 0.8$ V/nm, $T = 10$ fs, and $\sigma = 0.5T$. The sign of Q denotes the moving direction of the transferred charge, the positive values indicate the charge flowing from the left- to the right-hand side of the GNR, and negative values mean the opposite direction. Similar CEP dependence of Q has been found in previous works on junction systems [13,16,18]. In these works, the positive values of Q are usually different from the negative values because of the spatial dissymmetry of junction systems and the electrons tend toward moving in one direction compared to the other. In our calculation, however, the curve with positive values is the same as that with negative values due to the spatial symmetry of the GNR device. The maximum value of the transferred charge is given by $Q_{max} = 0.056e$, $0.097e$, $0.120e$, and $0.123e$ for different lengths $L = 6$, 8, 10, and 12, respectively. It can be seen that the charge Q_{max} increases significantly with lengths L. This relies on the fact that more photons have been adsorbed to generate a phototcurrent for the larger irradiation area.

Figure 5 shows the maximum transferred charge as a function of pulse duration time with width σ. The irradiation area is fixed at $L = 6$. As the duration time increases, Q_{max} decreases in the range of width σ varying from $0.3T$ to $1.0T$. At $\sigma = 1.0T$, the curve of Q_{max} reaches a minimum point with a value of approximately zero. In other words, this photon-driven transferred charge vanishes when the duration time of laser pulses is large enough. This is because the asymmetry of the electric field fades away with increasing σ and the external laser pulses tend to stable light illumination with a
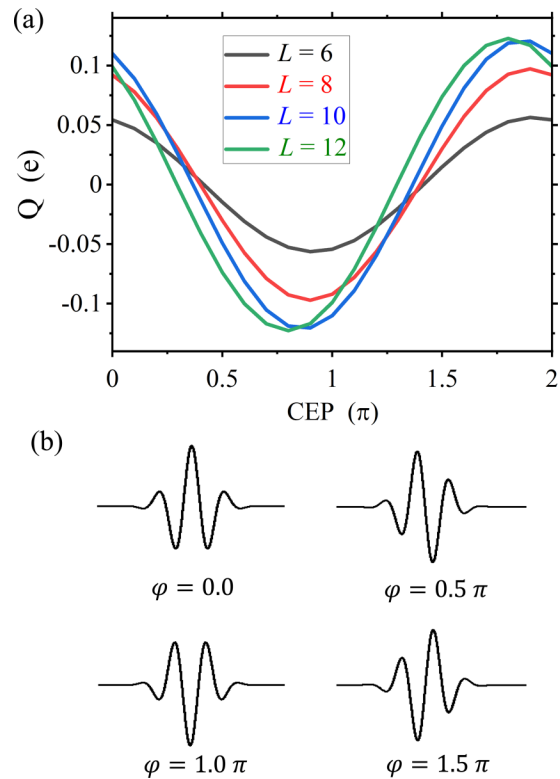

FIG. 4. (a) CEP dependence of transferred charge for different irradiation region lengths. (b) Scheme of the laser field for different CEP φ.
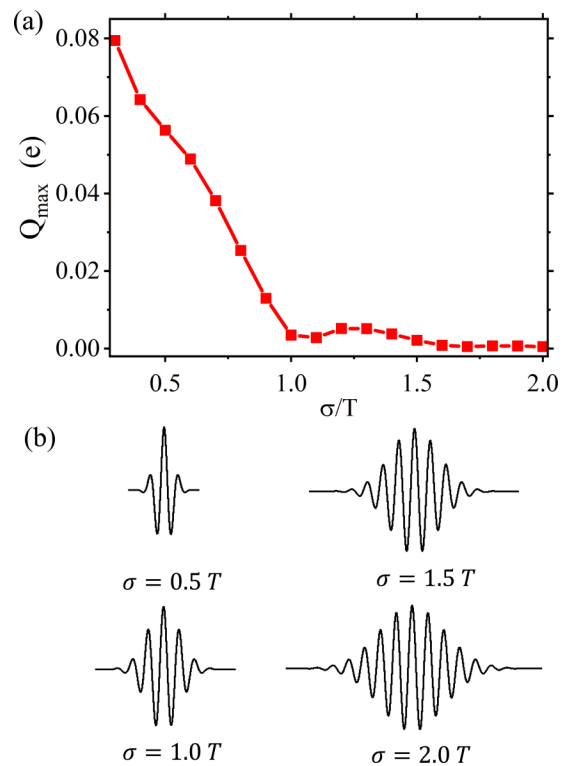

FIG. 5. (a) Maximum transferred charge as a function of duration time of pulses with width σ. (b) Scheme of the laser field for different widths σ with CEP $\varphi = 0$.
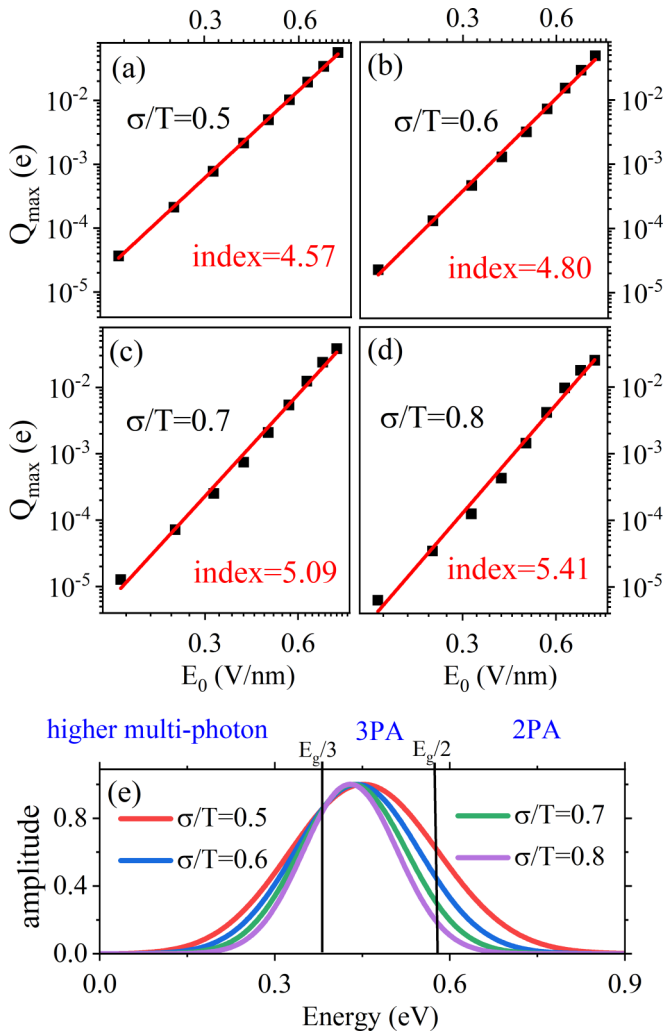
FIG. 6. Period time of pulses is set to $T = 10$ fs. (a)–(d) Simulation results (black points) of maximum transferred charge varying with the electric field amplitude E_0, and the fitting by power exponent $Q_{max} \propto E_0^r$ (red lines) for different duration times of pulses. The power indexes are 4.57, 4.80, 5.09, and 5.41 for $\sigma = 0.5T$, $0.6T$, $0.7T$, and $0.8T$, respectively. (e) Energy distribution of laser pulses; the distribution is divided into three regions by the energy values $E_g/2$ and $E_g/3$ with the band gap E_g of the GNR.
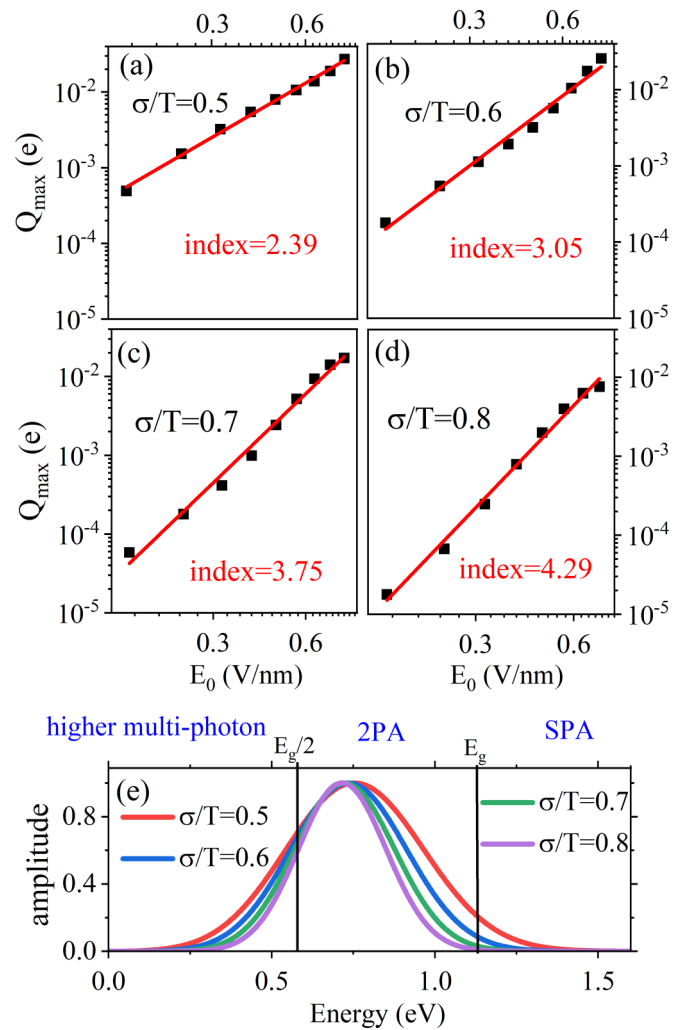
FIG. 7. Period time of pulses is changed to $T = 6$ fs. (a)–(d) Simulation results (black points) of maximum transferred charge, and the fitting by the power exponent (red lines). The power indexes are 2.39, 3.05, 3.75, and 4.29 for $\sigma = 0.5T$, $0.6T$, $0.7T$, and $0.8T$, respectively. (e) Energy distribution of laser pulses; the distribution is divided into three regions by the energy values E_g and $E_g/2$.

constant electric field amplitude. In this case, the generation of photocurrent needs an additional driving force, such as the built-in electric field in the *p-n* junctions. Note that we are focused on the transferred charge (time-integrated photocurrent) directly induced by the laser pulses in pure GNRs; thus, the width is always set to $\sigma < 1.0T$ in the present work.

C. Multiphoton absorption process induced by laser pulses

To understand the origin of transferred charge, we calculate the Q_{max} varying with the electric field amplitude E_0. Here, instead of CEP-dependent Q, we adopt Q_{max} to avoid the influence of the CEP. The period time of pulses is set to $T = 10$ fs. The simulation results (black points) are plotted in Fig. 6(a) for $\sigma = 0.5T$ on a log-log scale and are fitted by the following power exponent: $Q_{max} \propto E_0^r$ (red line). It is clear that the

charge Q_{max} has a power-exponent relation to field amplitude with a power index $r = 4.57$. The noninteger number of multiphoton excitation is due to the classical approximation of laser fields in our simulation. Results indicate that two- (2PA) and three-photon absorption (3PA) processes play dominant roles in the generation of the photocurrent. This conclusion can also be observed from the energy distribution of the laser pulses, which is given by the Fourier transform of the time-varying electric field and remain unchanged for different CEPs of the pulses. The red line in Fig. 6(e) shows the energy distribution for $\sigma = 0.5T$. From Fig. 1(b), the band gap of a seven-armchair GNR is found to be $E_g = 1.14$ eV; this band gap is consistent with the previous simulation results [23,46]. Thus, the energy distribution can be divided into three regions: 2PA ($E_g > E > E_g/2$), 3PA ($E_g/2 > E > E_g/3$) and higher multiphoton absorption ($E_g/3 > E$). The photon absorption is more likely to occur at the lower multiphoton absorption

region, so the transferred charge mainly originates from 2PA and 3PA.

Similarly, we also calculate the Q_{max} for different pulse duration times with the widths $\sigma = 0.6, 0.7$, and $0.8T$ [Figs. 6(b) to 6(d)], which have been fitted by power exponents. It can be seen that the power index grows gradually from 4.57 to 5.41, which means that the multiphoton absorption varies from a 2PA process to a 3PA process. The reason for this change is the adjustment of the energy distribution according to the pulse duration time, as shown in Fig. 6(e). The increase of duration time narrows the range of energy distribution to the 3PA region, and the distribution in the 2PA region becomes increasingly smaller. This would lead to the dominant contribution of photocurrent generation changing from a 2PA process to a 3PA process.

To further examine multiphoton absorption, the period time of pulses is changed to $T = 6$ fs and the central frequency 0.69 eV is adjusted to the 2PA region. Figures 7(a) to 7(d) show the simulation results of maximum transferred charge Q_{max} and the fitting by power exponents for different duration times. The power indexes are found to be 2.39, 3.05, 3.75, and 4.29 for $\sigma = 0.5T, 0.6T, 0.7T$, and $0.8T$, respectively. Figure 7(e) shows the corresponding energy distribution of the laser pulses. The distribution is divided into the following three regions by the energies E_g and $E_g/2$: single-photon absorption (SPA), 2PA, and higher multiphoton absorption. At $\sigma = 0.5T$, the photon absorption mainly occurs in the SPA process due to a significant distribution in that region [red line in Fig. 7(e)]. With increasing width σ, it can be seen that the origin of Q_{max} changes from the SPA process to the 2PA process since the power index changes from 2.39 to 4.29. This relies on the fact that the range of energy distribution is narrowing into the 2PA region [Fig. 7(e)], and thus the distribution in the SPA region becomes increasingly smaller. For $\sigma = 0.8T$, the photon absorption completely turns into the 2PA process because of the vanishing of distribution in the SPA region.

It can also be seen that the transient photocurrent in a GNR is mainly driven by multi-photon absorption, especially for a laser pulse with a smaller central frequency compared to the band gap. The order of multiphoton absorption is determined by the energy distribution of laser pulses and by the band gap of the system. A similar phenomenon was found in previous work on photocurrents in dielectrics [47].

IV. CONCLUSION

In this study, we employed the TD-NEGF approach to simulate the electron dynamics driven by few-cycle laser pulses in pure armchair GNRs. The transferred charge can be controlled by the waveform of the pulses, such as the CEP, duration time, electric field amplitude, and period time of the incident laser. When the duration is short enough ($\sigma < 1.0T$), the transferred charge is clearly dependent on the CEP due to the asymmetry of the electric field. With increasing duration time, the asymmetry of the electric field fades away and the transferred charge induced by the laser pulse gradually vanishes. From the calculation results of Q_{max} varying with the electric field amplitude, it can be seen that the origin of transferred charge comes from the multiphoton absorption process. The order of the photon absorption can be controlled from SPA to 3PA by adjusting the energy distribution of the laser pulses.

[1] F. Krausz and M. Ivanov, Attosecond physics, Rev. Mod. Phys. **81**, 163 (2009).

[2] M. F. Ciappina, J. A. Pérez-Hernández, A. S. Landsman, W. A. Okell, S. Zherebtsov, B. Förg, J. Schötz, L. Seiffert, T. Fennel, T. Shaaran *et al.*, Attosecond physics at the nanoscale, Rep. Prog. Phys. **80**, 054401 (2017).

[3] F. Calegari, D. Ayuso, A. Trabattoni, L. Belshaw, S. De Camillis, S. Anumula, F. Frassetto, L. Poletto, A. Palacios, P. Decleva *et al.*, Ultrafast electron dynamics in phenylalanine initiated by attosecond pulses, Science **346**, 336 (2014).

[4] C. M. Liu, J. Manz, K. Ohmori, C. Sommer, N. Takei, J. C. Tremblay, and Y. Zhang, Attosecond Control of Restoration of Electronic Structure Symmetry, Phys. Rev. Lett. **121**, 173201 (2018).

[5] S. Sederberg, D. Zimin, S. Keiber, F. Siegrist, M. S. Wismer, V. S. Yakovlev, I. Floss, C. Lemell, J. Burgdörfer, M. Schultze *et al.*, Attosecond optoelectronic field measurement in solids, Nat. Commun. **11**, 430 (2020).

[6] Y. Bai, L. Song, R. Xu, C. Li, P. Liu, Z. Zeng, Z. Zhang, H. Lu, R. Li, and Z. Xu, Waveform-Controlled Terahertz Radiation from the Air Filament Produced by Few-Cycle Laser Pulses, Phys. Rev. Lett. **108**, 255004 (2012).

[7] M. Clerici, M. Peccianti, B. E. Schmidt, L. Caspani, M. Shalaby, M. Giguere, A. Lotti, A. Couairon, F. Légaré, T. Ozaki *et al.*, Wavelength Scaling of Terahertz Generation by Gas Ionization, Phys. Rev. Lett. **110**, 253901 (2013).

[8] J. Déchard, X. Davoine, and L. Bergé, THz Generation from Relativistic Plasmas Driven by Near- to Far-Infrared Laser Pulses, Phys. Rev. Lett. **123**, 264801 (2019).

[9] T. L. Cocker, D. Peller, P. Yu, J. Repp, and R. Huber, Tracking the ultrafast motion of a single molecule by femtosecond orbital imaging, Nature (London) **539**, 263 (2016).

[10] S. Li, S. Chen, J. Li, R. Wu, W. Ho *et al.*, Joint Space-Time Coherent Vibration Driven Conformational Transitions in a Single Molecule, Phys. Rev. Lett. **119**, 176002 (2017).

[11] M. Garg and K. Kern, Attosecond coherent manipulation of electrons in tunneling microscopy, Science **367**, 411 (2020).

[12] Y. Kwok, G. Chen, and S. Mukamel, STM imaging of electron migration in real space and time: A simulation study, Nano Lett. **19**, 7006 (2019).

[13] R. Wang, F. Bi, W. Lu, X. Zheng, and C. Yam, Tracking electron dynamics of single molecules in scanning tunneling microscopy junctions with laser pulses, J. Phys. Chem. Lett. **12**, 6398 (2021).

[14] M. Ludwig, G. Aguirregabiria, F. Ritzkowsky, T. Rybka, D. C. Marinica, J. Aizpurua, A. G. Borisov, A. Leitenstorfer, and D. Brida, Sub-femtosecond electron transport in a nanoscale gap, Nat. Phys. **16**, 341 (2020).

[15] K. Yoshioka, I. Katayama, Y. Minami, M. Kitajima, S. Yoshida, H. Shigekawa, and J. Takeda, Real-space coherent manipulation of electrons in a single tunnel junction by single-cycle terahertz electric fields, Nat. Photonics **10**, 762 (2016).

[16] L. Chen, Y. Zhang, G. Chen, and I. Franco, Stark control of electrons along nanojunctions, Nat. Commun. **9**, 1 (2018).

[17] K. Yoshioka, I. Katayama, Y. Arashida, A. Ban, Y. Kawada, K. Konishi, H. Takahashi, and J. Takeda, Tailoring single-cycle near field in a tunnel junction with carrier-envelope phase-controlled terahertz electric fields, Nano Lett. **18**, 5198 (2018).

[18] Z. Hu, Y. Kwok, G. Chen, and S. Mukamel, Carrier-envelope-phase modulated currents in scanning tunneling microscopy, Nano Lett. **21**, 6569 (2021).

[19] H. Wang, H. S. Wang, C. Ma, L. Chen, C. Jiang, C. Chen, X. Xie, A.-P. Li, and X. Wang, Graphene nanoribbons for quantum electronics, Nat. Rev. Phys. **3**, 791 (2021).

[20] J. Cai, P. Ruffieux, R. Jaafar, M. Bieri, T. Braun, S. Blankenburg, M. Muoth, A. P. Seitsonen, M. Saleh, X. Feng *et al.*, Atomically precise bottom-up fabrication of graphene nanoribbons, Nature (London) **466**, 470 (2010).

[21] R. K. Houtsma, J. de la Rie, and M. Stöhr, Atomically precise graphene nanoribbons: Interplay of structural and electronic properties, Chem. Soc. Rev. **50**, 6541 (2021).

[22] Y.-W. Son, M. L. Cohen, and S. G. Louie, Half-metallic graphene nanoribbons, Nature (London) **444**, 347 (2006).

[23] Y.-W. Son, M. L. Cohen, and S. G. Louie, Energy Gaps in Graphene Nanoribbons, Phys. Rev. Lett. **97**, 216803 (2006).

[24] W. Han, R. K. Kawakami, M. Gmitra, and J. Fabian, Graphene spintronics, Nat. Nanotechnol. **9**, 794 (2014).

[25] L. Yang, C.-H. Park, Y.-W. Son, M. L. Cohen, and S. G. Louie, Quasiparticle Energies and Band Gaps in Graphene Nanoribbons, Phys. Rev. Lett. **99**, 186801 (2007).

[26] H. Raza and E. C. Kan, Armchair graphene nanoribbons: Electronic structure and electric-field modulation, Phys. Rev. B **77**, 245434 (2008).

[27] A. Kimouche, M. M. Ervasti, R. Drost, S. Halonen, A. Harju, P. M. Joensuu, J. Sainio, and P. Liljeroth, Ultra-narrow metallic armchair graphene nanoribbons, Nat. Commun. **6**, 10177 (2015).

[28] R. Wang, F. Bi, W. Lu, and C. Yam, Tunable photoresponse by gate modulation in bilayer graphene nanoribbon devices, J. Phys. Chem. Lett. **10**, 7719 (2019).

[29] D. A. Stewart and F. Léonard, Photocurrents in Nanotube Junctions, Phys. Rev. Lett. **93**, 107401 (2004).

[30] E. C. Peters, E. J. Lee, M. Burghard, and K. Kern, Gate dependent photocurrents at a graphene p–n junction, Appl. Phys. Lett. **97**, 193102 (2010).

[31] J. Chen, Y. Hu, and H. Guo, First-principles analysis of photocurrent in graphene p n junctions, Phys. Rev. B **85**, 155441 (2012).

[32] G. Wang, M. Zhang, D. Chen, Q. Guo, X. Feng, T. Niu, X. Liu, A. Li, J. Lai, D. Sun *et al.* Seamless lateral graphene p–n junctions formed by selective in situ doping for high-performance photodetectors, Nat. Commun. **9**, 5168 (2018).

[33] X. Zheng, F. Wang, C. Y. Yam, Y. Mo, and G. H. Chen, Time-dependent density-functional theory for open systems, Phys. Rev. B **75**, 195127 (2007).

[34] C. Y. Yam, X. Zheng, G. H. Chen, Y. Wang, T. Frauenheim, and T. A. Niehaus, Time-dependent versus static quantum transport simulations beyond linear response, Phys. Rev. B **83**, 245448 (2011).

[35] S. Chen, Y. Kwok, and G. Chen, Time-dependent density functional theory for open systems and its applications, Acc. Chem. Res. **51**, 385 (2018).

[36] X. Zheng, G. Chen, Y. Mo, S. Koo, H. Tian, C. Yam, and Y. Yan, Time-dependent density functional theory for quantum transport, J. Chem. Phys. **133**, 114101 (2010).

[37] R. Wang, D. Hou, and X. Zheng, Time-dependent density-functional theory for real-time electronic dynamics on material surfaces, Phys. Rev. B **88**, 205126 (2013).

[38] Y. H. Kwok, H. Xie, C. Y. Yam, X. Zheng, and G. H. Chen, Time-dependent density functional theory quantum transport simulation in non-orthogonal basis, J. Chem. Phys. **139**, 224111 (2013).

[39] H. Xie, F. Jiang, H. Tian, X. Zheng, Y. Kwok, S. Chen, C. Yam, Y. Yan, and G. Chen, Time-dependent quantum transport: An efficient method based on liouville-von-neumann equation for single-electron density matrix, J. Chem. Phys. **137**, 044113 (2012).

[40] R. Wang, X. Zheng, Y. Kwok, H. Xie, G. Chen, and C. Yam, Time-dependent density functional theory for open systems with a positivity-preserving decomposition scheme for environment spectral functions, J. Chem. Phys. **142**, 144112 (2015).

[41] R. Wang, W. Lu, H. Xie, X. Zheng, and C. Yam, Theoretical investigation of real-time charge dynamics in open systems coupled to bulk materials, J. Chem. Phys. **150**, 174119 (2019).

[42] Y. Zhang, S. Chen, and G. H. Chen, First-principles time-dependent quantum transport theory, Phys. Rev. B **87**, 085110 (2013).

[43] M. L. Sancho, J. L. Sancho, J. L. Sancho, and J. Rubio, Highly convergent schemes for the calculation of bulk and surface green functions, J. Phys. F: Met. Phys. **15**, 851 (1985).

[44] A. H. Castro Neto, F. Guinea, N. M. R. Peres, K. S. Novoselov, and A. K. Geim, The electronic properties of graphene, Rev. Mod. Phys. **81**, 109 (2009).

[45] R. Alvarez-Puebla, L. M. Liz-Marzán, and F. J. García de Abajo, Light concentration at the nanometer scale, J. Phys. Chem. Lett. **1**, 2428 (2010).

[46] Q. Sun, Y. Yan, X. Yao, K. Müllen, A. Narita, R. Fasel, and P. Ruffieux, Evolution of the topological energy band in graphene nanoribbons, J. Phys. Chem. Lett. **12**, 8679 (2021).

[47] S. Y. Kruchinin, M. Korbman, and V. S. Yakovlev, Theory of strong-field injection and control of photocurrent in dielectrics and wide band gap semiconductors, Phys. Rev. B **87**, 115201 (2013).